



HAL
open science

Detailed Redox Mechanism and Self-Discharge Diagnostic of 4.9 V $\text{LiMn}_{1.5}\text{Ni}_{0.5}\text{O}_4$ Spinel Cathode revealed by Raman Spectroscopy

Ankush Bhatia, Yosra Dridi Zrelli, Jean Pierre Pereira-Ramos, Rita Baddour-Hadjean

► **To cite this version:**

Ankush Bhatia, Yosra Dridi Zrelli, Jean Pierre Pereira-Ramos, Rita Baddour-Hadjean. Detailed Redox Mechanism and Self-Discharge Diagnostic of 4.9 V $\text{LiMn}_{1.5}\text{Ni}_{0.5}\text{O}_4$ Spinel Cathode revealed by Raman Spectroscopy. *Journal of Materials Chemistry A*, 2021, 9 (23), pp.13496-13505. 10.1039/D1TA00989C . hal-03280041

HAL Id: hal-03280041

<https://hal.science/hal-03280041>

Submitted on 7 Jul 2021

HAL is a multi-disciplinary open access archive for the deposit and dissemination of scientific research documents, whether they are published or not. The documents may come from teaching and research institutions in France or abroad, or from public or private research centers.

L'archive ouverte pluridisciplinaire **HAL**, est destinée au dépôt et à la diffusion de documents scientifiques de niveau recherche, publiés ou non, émanant des établissements d'enseignement et de recherche français ou étrangers, des laboratoires publics ou privés.

ARTICLE

Detailed Redox Mechanism and Self-Discharge Diagnostic of 4.9 V $\text{LiMn}_{1.5}\text{Ni}_{0.5}\text{O}_4$ Spinel Cathode revealed by Raman Spectroscopy

Ankush Bhatia,^{*a} Yosra Dridi Zrelli,^a Jean-Pierre Pereira-Ramos,^a and Rita Baddour-Hadjean,^{*a}

Received 00th January 20xx,
Accepted 00th January 20xx

DOI: 10.1039/x0xx00000x

Lithium-ion batteries are commonly used for electrical energy storage in portable devices and are promising systems for large-scale energy storage. However, their application is still limited due to electrode degradation and stability issues. To enhance the fundamental understanding of electrode degradation, we report on the Raman spectroscopic characterization of the promising 5 V spinel $\text{LiMn}_{1.5}\text{Ni}_{0.5}\text{O}_4$ (LMNO) composite cathode. The Raman spectral variations displayed during the charge-discharge cycle in the 3.5 V – 4.9 V vs. Li^+/Li potential range are shown to be strongly associated with the change in the transition metals valence states. A careful electrochemical and spectroscopic analysis allows identifying specific descriptors of the $\text{Ni}^{2+}/\text{Ni}^{3+}/\text{Ni}^{4+}$ species in the Raman spectra and providing their relative ratio during the redox process. This combined approach demonstrates the efficiency of Raman spectroscopy to determine the state of charge (SOC) of the LMNO cathode, paving the way for a fast and reliable measure of the self-discharge phenomenon in the spinel electrode.

Introduction

Developing cathode materials with high energy densities and long cyclability is one of the key challenges for implementing the lithium-ion battery (LIB) technology for the electric vehicles (EVs), hybrid electric vehicles (HEV) and plug-in hybrid electric vehicles (PHEV) applications.^{1–3} Among them, spinel LiMn_2O_4 (hereafter denoted LMO) and its derivatives have been extensively investigated as promising candidates because of their easy preparation, abundance, low cost and environmental friendliness properties.^{4–6} LMO is already commercialized but still suffers from poor cycling performance, especially at elevated temperatures due to the Jahn-Teller distortion as well as the disproportionation of Mn^{3+} and dissolution of Mn^{2+} in the electrolyte.⁷ Ni substitution in LiMn_2O_4 has been reported to be an effective method to solve the above problems.^{8–10} Thus, spinel $\text{LiMn}_{1.5}\text{Ni}_{0.5}\text{O}_4$ (hereafter denoted LMNO) is of great interest as cathode material for power LIBs since it offers a high voltage plateau at ~4.7 V vs. Li^+/Li , a specific capacity of ~135 mAh g^{-1} leading to a high energy density of 700 Wh kg^{-1} (20 and 30% greater than LiCoO_2 and LiFePO_4 , respectively).¹¹ Spinel LMNO has a robust cubic close-packed crystal structure made of edge-sharing MO_6 octahedra (M= Mn or Ni). The distribution of cations on the octahedral sites was found to depend on synthesis conditions. Ni and Mn have been proposed to either order in the *4a* and *12d* sites of an ordered $P4_332$ space group or be randomly

distributed in the *16d* sites of a disordered $Fd\bar{3}m$ -type unit cell.¹² Great efforts have been made to understand the fundamental chemistry and material issues of LMNO and propose modification strategies to overcome its intrinsic challenges for power LIBs, as introduced in detail in several papers.^{6,13,14} Particularly, it was pointed out that the most critical issue of LMNO is the high potential of these cathodes that leads to electrolyte decomposition and concurrent degradation reactions resulting in rapid capacity fade.¹⁵ The self-discharge has been a key issue even in commercialized Li-ion batteries, which refers to the loss of capacity under open circuit condition at the charged state.^{16,17} Many strategies have been reported in literature in order to slowdown the self-discharge process in LMNO. Among these, it is worth mentioning optimization of LMNO particles architecture, coating of the particles with a protecting material and modification of the electrolyte using different kinds of additives.^{18–27} One of the remarkable properties of LMNO is the structure-dependent redox reaction and phase transformation, the disordering of Ni/Mn affecting the phase transformation behaviour by extending the solid-solution reaction for extracting lithium. The disordered polymorph with an $Fd\bar{3}m$ symmetry is usually synthesized at 900 °C through a fast cooling process.¹⁴ The delithiation/lithiation mechanism of disordered LMNO has been investigated using mainly X-ray and neutron diffraction.^{28–38} These studies revealed that the disordered spinel has a large solid-solution region at low states-of-charge (L_xMNO , $0.5 < x < 1$)³¹, which is considered to be the main reason behind its superior rate capability compared to the ordered phase.³³ Although X-ray diffraction (XRD) and neutron diffraction provide a picture of the phase evolution during cycling, we still lack information about the

^aInstitut de Chimie et des Matériaux Paris-Est, UMR 7182 CNRS-UPEC, 2 rue Henri Dunant, F-94320, Thiais, France.

Electronic Supplementary Information (ESI) available: [details of any supplementary information available should be included here]. See DOI: 10.1039/x0xx00000x

atomic level variations during the electrochemical reaction of LMNO. The lithium local environment during charging has been studied in detail by ^6Li MAS NMR^{39,40} while evolution of the local structure around Mn^{4+} with lithium extraction has been carried out by EPR.⁴¹ Raman spectroscopy (RS) on the other hand is a highly versatile technique widely used to characterize electrode materials. A detailed analysis of the Raman spectra can infer lattice symmetry, coordination geometry, oxidation state, coexistence of several phases, presence of defects, impurities, strains and other phenomena relevant for the characterization of electrode materials for LIBs, as described in⁴². In particular, RS provides a unique direct probe of the M-O bonds in cathode materials, which are at the heart of their electrochemistry and govern their stability.⁴²⁻⁴⁴ A number of groups have applied Raman microscopy to understand the structure and structural evolution of various electrode materials for LIBs such as TiO_2 , V_2O_5 (bulk and thin film)⁴⁶⁻⁴⁸ as well as layered rock-salt-type $\text{Li}_x\text{M}_y\text{O}_z$ ($\text{M} = \text{Co}, \text{Ni}, \text{Al}, \text{Mn}$) compounds.⁴⁹⁻⁵⁵ The pioneering *in situ* Raman microscopy study of Kostecki et al.⁴⁹ on $\text{LiNi}_{0.8}\text{Co}_{0.15}\text{Al}_{0.05}\text{O}_2$ (NCA) showed that the Raman spectral signature of NCA is sensitive to the compositional changes, which provides a spectroscopic measure of the SOC of oxide particles in the composite cathode. Later on, Nanda et al. performed micrometer-resolved mapping to measure spatial variations of the SOC at macroscopic length scale of the NCA composite electrodes.⁵⁰ More recently, Berg et al.⁵¹ carried out *operando* Raman spectroscopy experiments to rationalize the relationships between the spectral response of NCA and the electrochemistry. Using complementary *operando* techniques and DFT calculations, a picture of the bond character evolution during charge-discharge was provided through the analysis of the M-O band position and intensity, whereas the appearance of new modes was associated to the formation of Li^+ vacancies. Several papers have also reported Raman spectra of Li-Mn-rich layered oxides, with considerable variety in terms of both the observed vibrational features and their interpretation.⁵²⁻⁵⁵ *In-situ* Raman on $\text{Li}_{1.2}\text{Mn}_{0.54}\text{Ni}_{0.13}\text{Co}_{0.13}\text{O}_2$ composite cathode revealed lithium extraction through the presence of a new Raman band at 543 cm^{-1} ascribed to the oxidation of Ni^{2+} ions.⁵² More recently, *operando* Raman spectroscopy experiments on $\text{Li}_x\text{Ni}_{1-2y}\text{Co}_y\text{Mn}_y\text{O}_2$ ($y=0.1, 0.2, 0.33$) composite electrodes during cycling reported that Ni oxidation occurs as a stepwise $\text{Ni}^{2+} \leftrightarrow \text{Ni}^{3+} \leftrightarrow \text{Ni}^{4+}$ process, with distinct $\text{Ni}^{2+}\text{-O}$ and $\text{Ni}^{4+}\text{-O}$ environments detected through the 609 cm^{-1} band and a band triplet at 480, 555 and 575 cm^{-1} , respectively.⁵⁴ However, to our knowledge, very few papers have reported Raman spectroscopic studies on spinel-based LMNO during charge-discharge.⁵⁶⁻⁵⁷ An *in situ* Raman spectroscopic investigation on (Cr, Co) doped LMNOs reports as major conclusion the detection of a new band at 538 cm^{-1} at the end of the charge.⁵⁶ Similarly, the other study performed on LMNO thin film shows a new Raman band at 540 cm^{-1} appearing around 4.7 V, assigned to the $\text{Ni}^{4+}\text{-O}$ stretching vibration.⁵⁷

In this work, RS is carried out for the first time to explore the short-range environment in a disordered LMNO cathode

during charge-discharge in the 3.5 – 4.9 V vs. Li^+/Li voltage range. Significant evolution of the Raman spectra is displayed during the electrochemical reaction, signifying a modification of the Ni-O bond strength directly related to changes in the Ni valence state. We demonstrate that an appropriate analysis of the Raman spectra enables a reliable determination of the electrode SOC, through a quantitative estimation of the Ni^{2+} , Ni^{3+} and Ni^{4+} relative contents in the LMNO cathode. As a proof of concept, we show the potential of Raman spectroscopy as an efficient and simple diagnostic tool to measure the self-discharge phenomenon occurring in the LMNO cathode.

Results and discussion

Structural characterization

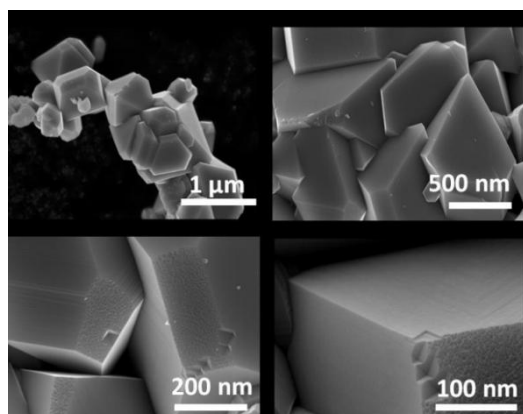


Figure 1. SEM images of as-prepared LMNO powder.

The SEM images of the as-synthesized powder show high-crystallized micrometric octahedral-shaped particles with smooth surfaces (Fig.1). The Rietveld refinement of XRD pattern of the as-synthesized powder (Fig.2a) corresponds to a spinel structure ($Fd\bar{3}m$ space group, JCPDS No 80-2162) consistent with the Ni/Mn disordered phase in which Ni and Mn are randomly distributed on $16d$ position, Li and O on $8a$ and $32e$ octahedral sites, respectively (see Fig.S1 and Table S1). The PND pattern (Fig.2b) unambiguously points to the formation of a pure disordered LMNO powder using the synthesis procedure described in the experimental section. The cubic close-packed LMNO crystal structure (Fig.S1) is made of edge-sharing MO_6 octahedra ($\text{M} = \text{Mn}$ or Ni) enabling 3D channels for high rate Li^+ conduction. The refined cubic lattice parameter $a = 8.18\text{ \AA}$ is in agreement with previously reported value.⁵⁸ The presence of weak intensity reflections at ca. $2\theta = 43.8^\circ$ and 51.3° (see enlarged view in Fig.S2) is due to small trace of rock salt Ni rich impurities (space group $Fm\bar{3}m$). The exact chemical composition of rock-salt impurities has not been determined yet but it has been suggested to be $\text{Li}_{1-x}\text{Ni}_x\text{O}$, $(\text{Li}_x\text{Mn}_{0.66}\text{Ni}_{0.34})_y\text{O}$ and/or Ni_6MnO_8 .⁵⁹ EDS-SEM analysis give an atomic Ni:Mn ratio of 1:2.9, with the presence of Ni rich

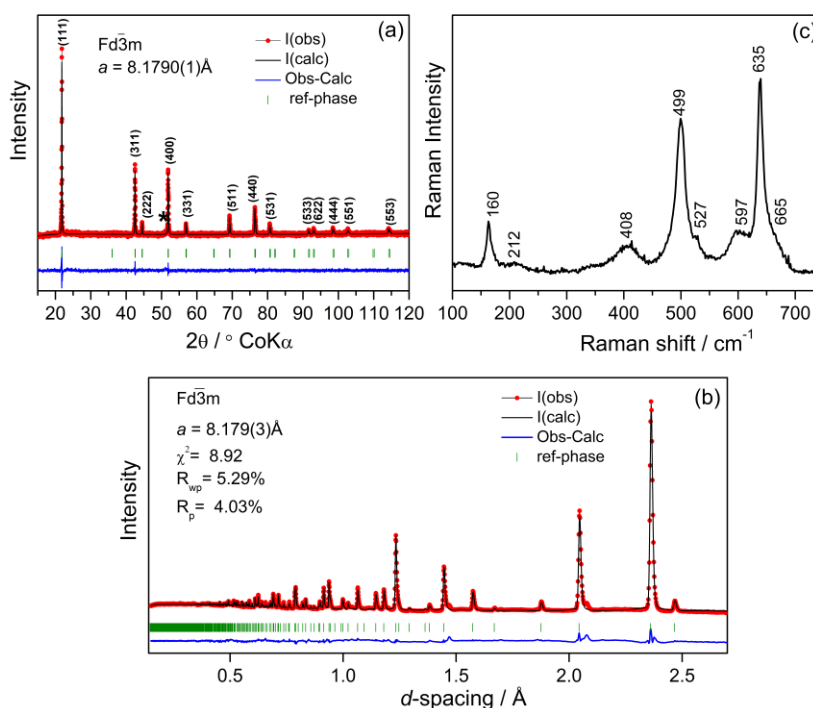


Figure 2. Rietveld refinement of XRD pattern, * rock salt phase (a); neutron diffraction pattern (b) and Raman spectrum (c) of as-prepared LMNO powder.

impurities randomly distributed on the different sites of the particles. The slight deviation from the expected 1:3 stoichiometry is due to oxygen loss at 900°C and the presence of Ni-rich impurities.

Raman spectroscopy is a relevant structural method to differentiate the ordered $P4_332$ and disordered $Fd\bar{3}m$ spinel structures since it is highly sensitive to the local symmetry of these two polymorphs. According to group theory, the number of expected Raman-active modes for the ordered spinel ($6A_{1g}+14E_g+22F_2$) is much larger than for the disordered phase ($A_{1g}+E_g+3F_{2g}$). The Raman spectrum of the as-prepared LMNO powder (**Fig.2c**) exhibits eight main bands located at 160, 212, 408, 499, 527, 597, 635 and 665 cm^{-1} typical of the $Fd\bar{3}m$ disordered structure. Indeed, the rich Raman fingerprint characteristic of ordering of the Ni^{2+} and Mn^{4+} species in space group $P4_332$, showing additional peaks at 221, 240, 251, 293, 325, 378 and 462 cm^{-1} is not detected.⁶⁰⁻⁶³ A full assignment of this Raman fingerprint can be provided by analogy with the parent compound LMO (**Table 1**).^{60,61}

	LMO	LMNO
$F_{2g}(1)$	163	160/212
E_g	342	408
$F_{2g}(2)$	421	499/527
A_{1g}	578, 625	597/635
$F_{2g}(3)$	653	665

Table 1. Experimental Raman wavenumbers of LMO⁶⁰ and LMNO (in cm^{-1}) and their assignments.

The observation of a larger number of Raman bands (8) compared to those predicted (5) is mainly attributed to the introduction of Ni^{2+} and to the simultaneous existence of Mn^{3+}

and Mn^{4+} ions.^{60,62,63} The latter provoke stretching vibrations of both locally distorted MnO_6^{9-} and isotropic MnO_6^{8-} octahedra. The local Jahn-Teller related lattice distortions of Mn^{3+} cause a loss of translation invariance and a breakdown of the Raman selection rules. A common feature of high voltage spinel Raman spectra is the strong A_{1g} band between 550 and 650 cm^{-1} and a group of bands between 100 and 550 cm^{-1} of weaker intensity. Previous experimental^{60,64} and theoretical^{64,65} studies have shown the intense A_{1g} peak at 635 cm^{-1} corresponds to the stretching of the 16d site cations M–O bonds in the MO_6 octahedra (M = Mn, Ni). The splitting of this vibrational mode is ascribed to the stretching of the Mn^{4+} –O (at 597 cm^{-1}), and a mixture of Mn^{3+} –O and Ni^{2+} –O bonds at 635 cm^{-1} . The weak shoulder at 665 cm^{-1} has F_{2g} symmetry and originates from bending vibrations of the 16d cations M–O bonds. Another rather intense Raman active mode of F_{2g} symmetry is observed at 499 cm^{-1} with a weak additional component at 527 cm^{-1} . This $F_{2g}(2)$ mode is reported as a pure Ni–O stretching mode^{60,65} which suggests that its position and intensity should be impacted by a change in the oxidation state of Ni. The phonon line at 408 cm^{-1} corresponds to the E_g symmetrical M–O–M deformation mode.⁶⁵ Finally, the lowest energy $F_{2g}(1)$ phonons at 160 and 212 cm^{-1} are predominantly due to lattice translation modes.⁶⁶

Electrochemical Investigation

The discharge-charge profile of LMNO is also a good way for distinguishing between the ordered and disordered phases. **Fig.3** shows the charge-discharge cycling curves of our LMNO powder. The initial charge capacity of 135 mAh g^{-1} indicates the extraction of 0.92 Li/mole of spinel, in good agreement with the literature. The small shoulder phenomenon detected

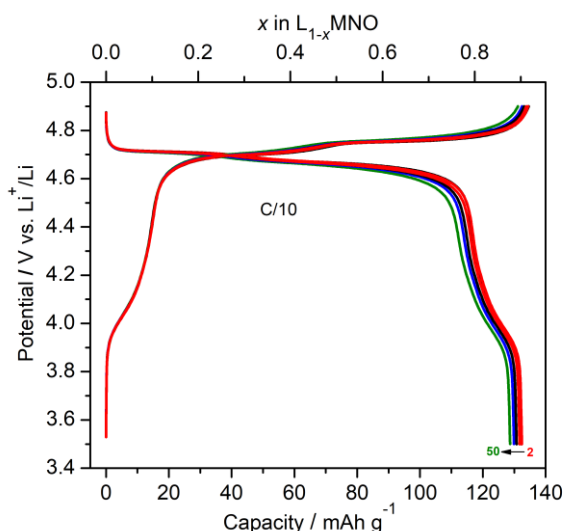


Figure 3. Charge-discharge cycles from the second cycle of the LMNO electrode, C/10 rate.

at ~ 4.1 V (involving a capacity of ~ 14 mAh g $^{-1}$) is attributed to the Mn $^{3+}$ /Mn $^{4+}$ redox couple. This electrochemical feature is typical of disordered LMNO and points to the presence of 0.1 Mn $^{3+}$ ions/mole of spinel formed during annealing at 900°C. The large plateau observed at higher voltage of 4.7 V – 4.8 V, involving a total capacity of ~ 121 mAh g $^{-1}$ (0.82 F/mole) is assigned to the Ni redox system.^{29,30,67} The slight deviation with the expected value of 1 F/mole is due to the presence of electrochemically inactive Ni-rich secondary rock-salt phases, leading to a lower Ni content in the spinel (≈ 0.41 /mole instead of 0.5), as previously reported.⁶⁸ The presence of two plateaus at 4.68 V and 4.75 V showing a well-marked potential separation of 70 mV is also an indication of the disordered nature of *Fd3m* LMNO, the Ni $^{2+}$ /Ni $^{3+}$ and Ni $^{3+}$ /Ni $^{4+}$ redox potentials and their gap being closely related to cation ordering on the 16*d* octahedral sites. This separation is reported to decrease from about 70 mV to around 20 mV, depending on the degree of ordering.^{29,30,68–71} The capacity value recovered in discharge (~ 133 mAh g $^{-1}$) indicates the good efficiency of the Li extraction/insertion reaction. An excellent capacity retention is observed even after 50 cycles at C/10 (96% i.e. ~ 129 mAh g $^{-1}$) with a coulombic efficiency of $\sim 98\%$. The present LMNO/Li half-cell exhibits similar electrochemical performance than that usually reported in the literature. Accordingly, the structural changes of this cathode material during the charge/discharge were further investigated using XRD and Raman spectroscopy.

Structural study during charge-discharge

The full XRD patterns of L $_{1-x}$ MNO electrodes recorded at different x values ($0 \leq x < 1$) during charge-discharge as well as a magnification showing the (311) reflection (which is a good indicator of the cubic lattice parameter) are shown in **Figs. 4** and **5a**, respectively. The calculated lattice parameters of the observed phases as a function of x in L $_{1-x}$ MNO are given in **Fig. 5b**. During charge, several lines such as the (311), (440) and

(444) peaks gradually shift toward higher angles, indicating lithium extraction through a solid solution of the pristine phase (phase 1) with decreasing cubic lattice parameter (from 8.18 to 8.09 Å, see **Fig. 5b**). A second cubic phase (phase 2) with a lower lattice constant of 8.01 Å appears when more than 50% of the Li $^{+}$ was deintercalated from LMNO, i. e. at Li content near 0.4 ($x = 0.6$). Both phases coexist up to the end of the charge, with nearly constant lattice parameter in this diphasic domain. Hence, the lithium deintercalation mechanism consists in a solid solution for $0 \leq x < 0.6$, followed by a diphasic region in which L $_{0.4}$ MNO (phase 1) and L $_{0.08}$ MNO (phase 2) coexist. The two processes are reversible upon discharge. This one-step-transition mechanism where the first diphasic reaction has been completely suppressed is typical of a cation-disordered LMNO spinel³⁴ and is consistent with previous studies reported for micrometric *Fd3m* LMNO spinel.^{27–30,33,34} The relative phase abundance of phase 1 (L $_{1-x}$ MNO with $0 \leq x \leq 0.6$) and phase 2 (L $_{0.08}$ MNO), estimated from the Rietveld analysis, is shown in **Fig. 5c**. The amount of the pristine cubic phase decreases from 80% for $x = 0.6$ to 20% for $x = 0.9$ while at the same time the phase 2 becomes dominant to be the unique phase for $x = 0.92$.

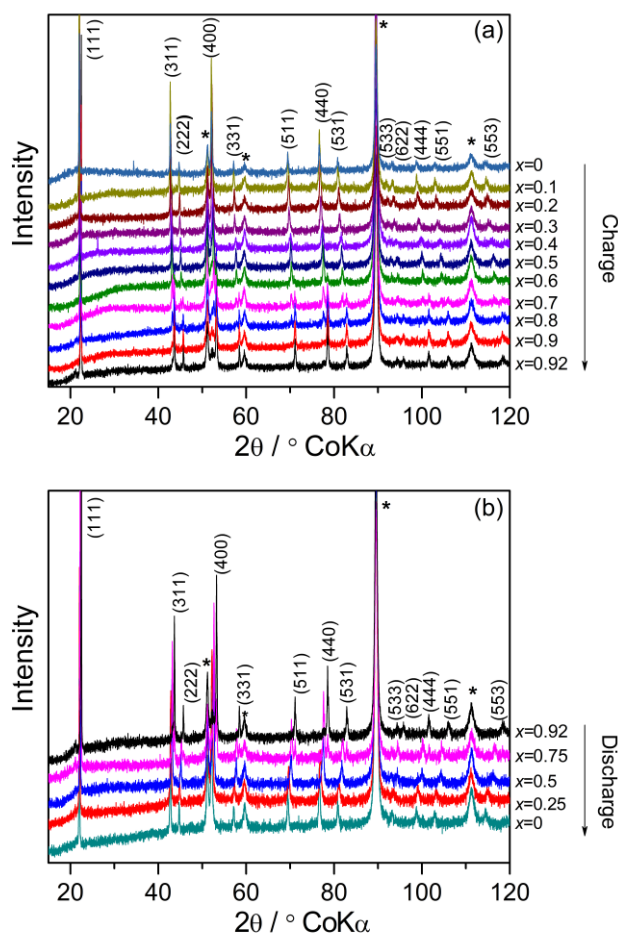


Figure 4. Ex-situ XRD patterns of the L $_{1-x}$ MNO electrode during the second cycle. Charge (a); Discharge (b), *sample holder.

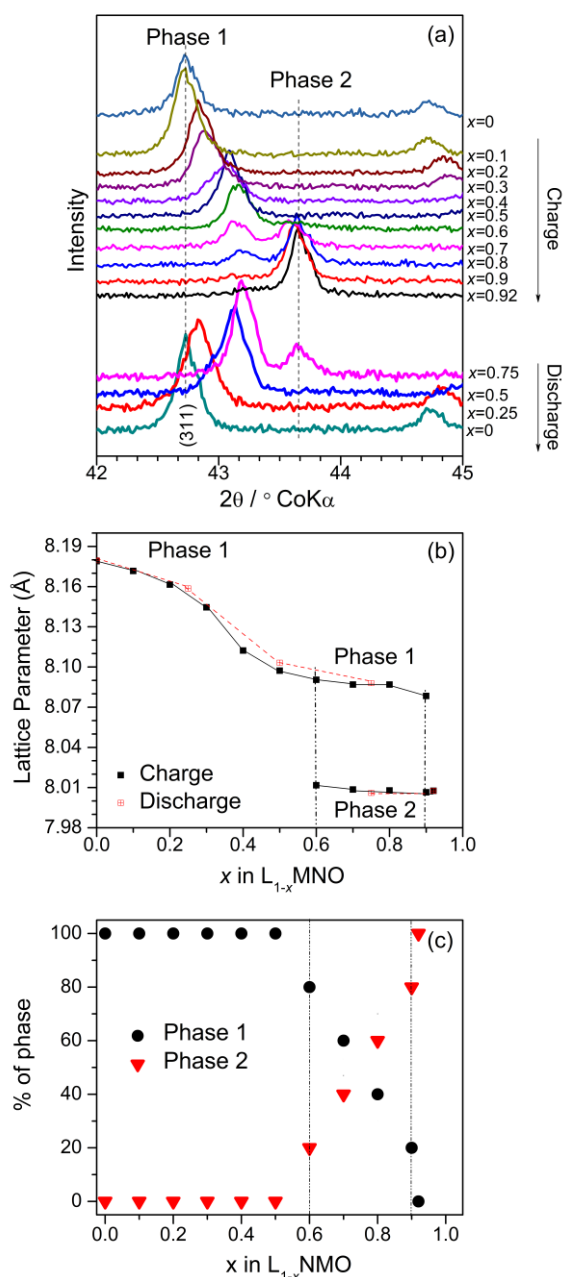


Figure 5. Enlarged view of the *ex-situ* XRD patterns of the $L_{1-x}\text{MNO}$ electrodes during charge and discharge showing the (311) reflection (a); Evolution of the cubic lattice parameter of the two phases during the charge (■) and the discharge (▣) (b); Relative phase abundance determined from Rietveld refinement of XRD patterns (c).

The Raman spectra of the same $L_{1-x}\text{MNO}$ electrodes recorded at different x values ($0 \leq x < 1$) during charge-discharge are shown in **Fig. 6**. Note that whatever the x value, similar spectra were found for the 10 investigated points, which indicates the good homogeneity of the electrodes. As shown in **Fig. 6a**, the Raman spectrum of the initial LMNO electrode, with Raman

bands at 160, 212, 408, 499, 527, 597, 635 and 665 cm^{-1} , is not altered for $x = 0.1$. This indicates that the $\text{Mn}^{3+} \rightarrow \text{Mn}^{4+}$ oxidation reaction does not induce noticeable change in the M–O bond lengths. However, from $x = 0.2$, the spectral profile is progressively modified, especially in the $450\text{--}700 \text{ cm}^{-1}$ region corresponding to the $F_{2g}(2)$ and A_{1g} modes. In so far as the $F_{2g}(2)$ mode is assigned to pure Ni–O stretching vibrations while the A_{1g} one involves mixed Mn, Ni vibrations in the MO_6 octahedra, the $F_{2g}(2)$ mode should be a relevant descriptor of the Ni–O bond upon lithium extraction. Indeed, **Fig. 6a** shows that this component is strongly affected from $x = 0.2$, i.e. as soon as the charge process involves the nickel redox system. In the $0.2 \leq x < 0.6$ composition range, the band at 499 cm^{-1} progressively disappears while the relative intensity of the weak component at 527 cm^{-1} increases to become practically the unique feature in the $F_{2g}(2)$ region for $x = 0.5$. Then, from $x = 0.6$, a new component emerges at 542 cm^{-1} and increases at the expense of the 527 cm^{-1} band during the second half of the charge ($0.6 \leq x < 1$). At the end of the charge ($x = 0.92$), the Raman spectrum exhibits a sole high intensity peak at 542 cm^{-1} in the $F_{2g}(2)$ region. These whole observations clearly indicate that the band evolution in the $F_{2g}(2)$ region is precisely related to the increase in the Ni oxidation state from +2 to +4 upon charge. The increasing wavenumber (e.g. $499/527/542 \text{ cm}^{-1}$) of the $F_{2g}(2)$ mode reflects a decrease in the Ni–O bond length with Li extraction (from 2.07 to 1.88 \AA from $x = 0$ to $x \approx 1$).^{72,73} It is then reasonable to assign the 499 , 527 and 542 cm^{-1} Raman bands to the $\text{Ni}^{2+}\text{--O}$, $\text{Ni}^{3+}\text{--O}$ and $\text{Ni}^{4+}\text{--O}$ stretching vibrations, respectively. Hence, the $0.1 < x < 0.6$ composition range belonging to the solid solution region is associated with the $\text{Ni}^{2+}/\text{Ni}^{3+}$ redox couple while the two-phase domain evidenced for $0.6 \leq x < 1$ corresponds to the $\text{Ni}^{3+}/\text{Ni}^{4+}$ system. Reverse trends are displayed during the discharge (**Fig. 6b**) and the complete restoration of the Raman spectrum of LMNO is observed after one cycle, with main bands at 164, 408, 500, 597 and 635 cm^{-1} . This result demonstrates the good reversibility of the lithium extraction-insertion process at the scale of the chemical bond.

Further quantitative information is accessible through the analysis of the Raman relative intensities in the $450\text{--}700 \text{ cm}^{-1}$ wavenumber range. Indeed, the Raman spectrum profile in the $F_{2g}(2)$ region is directly linked to the proportion of Ni^{2+} , Ni^{3+} and Ni^{4+} species in the cathode, estimated from the relative areas of the $F_{2g}(\text{Ni}^{2+})$, $F_{2g}(\text{Ni}^{3+})$ and $F_{2g}(\text{Ni}^{4+})$ components. Raman spectra fittings shown in **Fig. 7** lead then to the quantification of the different Ni redox species in the cathode (**Table 2**), i.e. its composition during the electrochemical reaction.

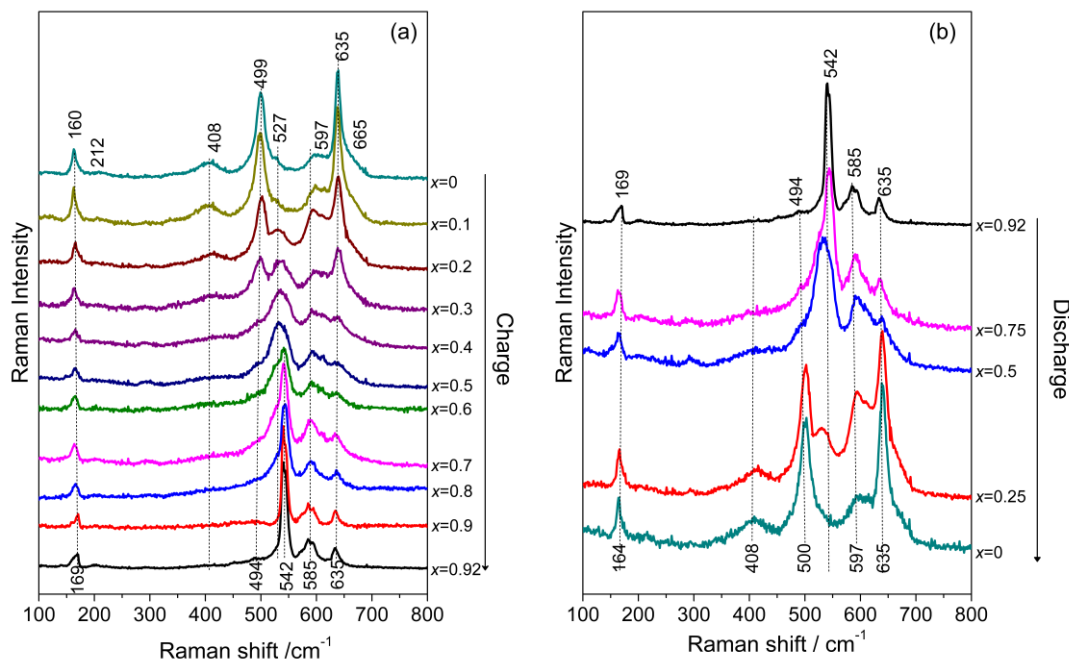


Figure 6. Ex situ Raman spectra of the $L_{1-x}MNO$ composite electrode during the second cycle. Charge (a); Discharge (b).

	x in $L_{1-x}MNO$	Ni^{2+} (%)	Ni^{3+} (%)	Ni^{4+} (%)
Charge	0	97	3	0
	0.2	73	27	0
	0.3	47	53	0
	0.4	34	66	0
	0.5	15	85	0
	0.6	0	89	11
	0.7	0	65	35
	0.85	0	33	67
	0.9	0	20	80
Discharge	0.75	0	61	39
	0.5	14	86	0
	0.25	73	27	0
	0.08	95	5	0

Table 2. Relative abundance of the Ni^{2+} , Ni^{3+} and Ni^{4+} species in the $L_{1-x}MNO$ electrodes during the second charge-discharge cycle calculated from Raman spectra fittings.

Fig. 8 shows the evolution of the $Ni^{2+}/Ni^{3+}/Ni^{4+}$ ratio during the charge determined from the Raman analysis. In the $0 \leq x \leq 0.1$ composition range, there is no change in the Ni^{2+} relative amount because the first charge step observed at ~ 4.1 V is due to the oxidation of the 0.1 Mn^{3+} present in the disordered LMNO. Then, from $x > 0.1$, the $Ni^{2+} \rightarrow Ni^{3+}$ oxidation clearly takes place along the potential plateau at 4.7 V, as illustrated

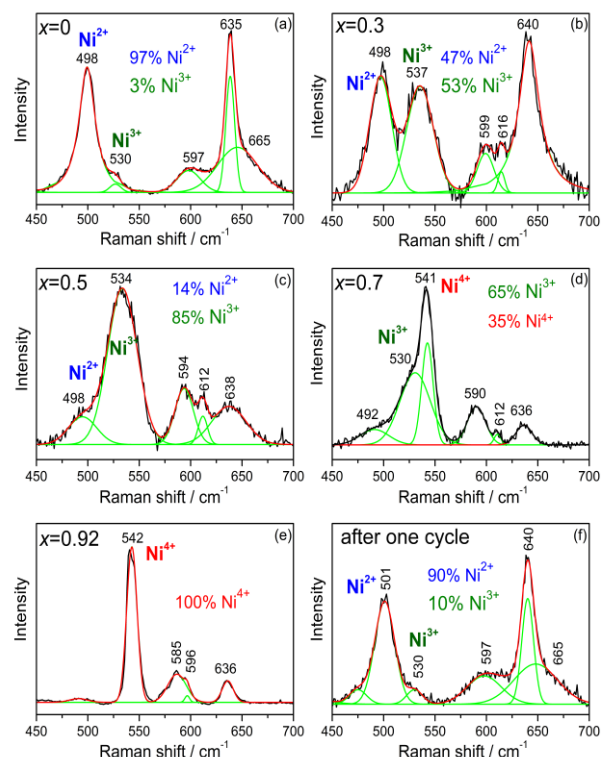


Figure 7. Raman spectra fittings (450-700 cm^{-1} region) of $L_{1-x}MNO$ composite electrodes at different SOC during the second charge and after the second charge-discharge cycle.

by the Raman spectra fitting clearly highlighting a decrease of the relative amount of Ni^{2+} content (see blue dashed line in Fig. 8) at the benefit of Ni^{3+} (green dashed line) in the $0.1 < x \leq 0.5$ composition range. Finally, a quantitative $Ni^{3+} \rightarrow Ni^{4+}$

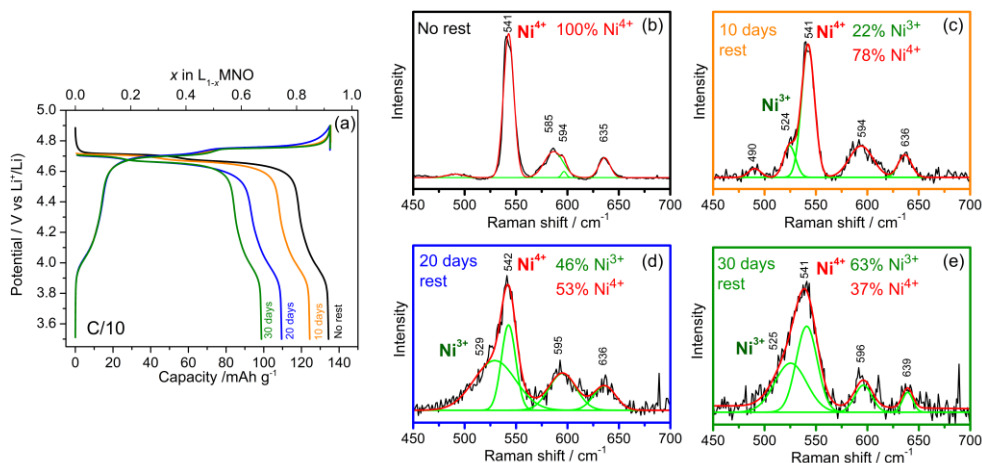


Figure 9. Effect of the self-discharge phenomenon on the electrochemical properties of LMNO (a) and Raman spectra of fully charged electrode: No rest (b), 10 days rest (c), 20 days rest (d), 30 days rest (e).

transformation occurs along the upper voltage plateau at 4.75 V ($x > 0.5$), manifesting itself through an abrupt decrease of the Ni^{3+} content at the benefit of Ni^{4+} species (red dashed line). The evolution of the $\text{Ni}^{2+}/\text{Ni}^{3+}/\text{Ni}^{4+}$ relative amounts as a function of x in L_{1-x}NMO electrodes estimated from Raman spectra fittings is very close to the expected one (Fig.S3), which demonstrates the reliability of the present Raman analysis and its efficiency to provide a good estimation of the electrode SOC.

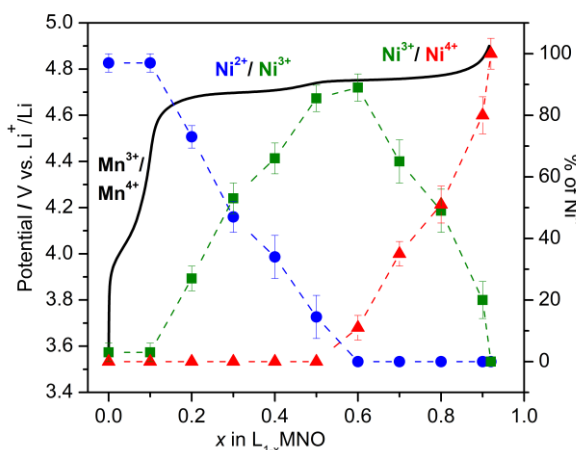


Figure 8. Galvanostatic charge profile of LMNO showing the different redox couples involved during the second charge. The evolution of the $\text{Ni}^{2+}/\text{Ni}^{3+}/\text{Ni}^{4+}$ ratio determined from the Raman spectra analysis are shown by dashed lines. Blue circles: Ni^{2+} , Green squares: Ni^{3+} , Red triangles: Ni^{4+} . The error bars correspond to statistical error of the deconvolution procedure.

To our knowledge, very few studies have attempted to characterize Li^+ insertion/extraction behavior of high voltage spinel using Raman spectroscopy^{56,57}. In both studies, *operando* Raman measurements lead to interfering signals from the electrolyte and only a new band at $538\text{--}540\text{ cm}^{-1}$ is

detected at the end of the charge, without any quantitative analysis being provided.

Self-discharge study

The present findings have prompted us to explore the degradation process that takes place when the cathode is delithiated. Indeed, it is known that spinel cathodes are prone to instability issues in their charged state, i. e. severe electrolyte oxidation associated to metal dissolution.^{15–17}

In order to characterize the occurrence of this so-called self-discharge phenomenon and to measure its kinetics, LMNO electrodes were charged at constant current (at C/10) till the potential 4.9 V vs. Li^+/Li then kept at zero current for varying rest times (10, 20 and 30 days). After this rest time, a constant current reduction is applied, leading to the discharge curves reported in Fig.9a. The obtained results confirm the occurrence of a self-discharge phenomenon at high voltage, the discharge capacity value of 135 mAh g^{-1} recovered without rest time decreasing to 124 mAh g^{-1} (8% loss), 110 mAh g^{-1} (18% loss) and 100 mAh g^{-1} (26% loss) after 10, 20 and 30 ageing days, respectively. The impact of the self-discharge phenomenon on the Raman spectra of charged electrodes is illustrated in Fig.9b-c-d-e. The Raman profile in the F_{2g} region is strongly modified, showing an additional component at $524\text{--}530\text{ cm}^{-1}$ whose relative intensity increases with the rest time of the fully charged electrode at the expense of the 541 cm^{-1} band.

Such evolution indicates a gradual reduction of Ni^{4+} into Ni^{3+} that can be quantitatively described based on Raman spectra fittings shown in Figs.9b-c-d-e. The obtained results (Table 3) show that the Raman analysis leads to estimated capacity losses in the range 3–8%, 13–17% and 23–27% after 10, 20, 30 days rest, respectively, very close to the values obtained from discharge tests, of 8, 18 and 26%, respectively.

Electrochemical analysis		Raman spectroscopy analysis				
Rest time (in days)	Capacity loss (%)	ν (Ni ³⁺ -O) (cm ⁻¹)	% Ni ³⁺	ν (Ni ⁴⁺ -O) (cm ⁻¹)	% Ni ⁴⁺	x in L _{1-x} MNO (loss)
0	0			542	100	0.92 (0)
10	8	524	22	541	78	0.86–0.89 (3–8%)
20	18	525	46	541	53	0.76–0.80 (13–17%)
30	26	529	63	542	37	0.67–0.71 (23–27%)

Table 3. Electrochemical and Raman spectroscopy analysis of the self-discharge phenomenon at high voltage of LMNO. No rest, 10, 20, and 30 days rest of the fully charged electrode in open circuit voltage.

Conclusions

In this study, we present Raman spectroscopy as an original and efficient tool to probe the local structure variations in a disordered LMNO cathode during lithium deintercalation/intercalation in the 3.5 V – 4.9 V voltage range. A complete assignment of the LMNO Raman spectrum is provided, allowing identifying reliable descriptors of the redox mechanism in LMNO at the level of the Ni–O bond. Significant variations in the Raman spectra are observed on the high voltage plateau at ~ 4.7 V, which are directly linked to the activity of the Ni redox species. Appropriate Raman spectra fitting performed at different state of charge and discharge lead to Ni²⁺/Ni³⁺/Ni⁴⁺ relative amounts that are found very consistent with the electrode SOC. As a proof of concept, the Raman study of fully charged electrodes kept at rest up to 30 days successfully pictures the unstable nature of Ni⁴⁺ ions and provides a fast, reliable and quantitative measure of the self-discharge phenomenon.

Experimental

Synthesis

LMNO powder was synthesized using the co-precipitation route that provides good crystallinity of the Fd3m phase.^{58,60} Stoichiometric amounts of lithium, nickel and manganese acetate (100% Aldrich) were dissolved in distilled water and stirred for 30 minutes. An oxalic-acid solution (1:1 molar ratio of oxalic acid to metal ions) was then added drop-wise under stirring to obtain a green precipitate. The precipitate solution was continuously stirred for 30 minutes before kept for overnight drying at 110°C. The obtained powder was pressed into pellets and preheated at 490°C to remove the carbonates in excess. The resulting powder was pelletized again and heated at 900°C for 96 h in air at 5°C/min.

Characterizations

Crystal structures were determined using X-ray and neutron diffraction as well as Raman spectroscopy. XRD experiments

were performed using a Panalytical XPert pro apparatus equipped with a X'Celerator detector and a CoK α radiation ($\lambda K\alpha = 1.789 \text{ \AA}$). All the diffraction patterns were collected with a 2θ step of 0.0167° . The as-collected patterns have been analyzed using Rietveld refinement method with the GSAS ExpGUI package.^{67,68} Neutron diffraction data were collected at room temperature on the POLARIS medium resolution time-of-flight (TOF) powder diffractometer at the ISIS spallation neutron source, Rutherford Appleton Laboratory (RAL), U.K. The experimental conditions of TOF are detailed in⁶⁹. Raman spectra were recorded with a LaBRAM HR 800 (Jobin-Yvon-Horiba) Raman micro-spectrometer including Edge filters and equipped for signal detection with a back illuminated charge coupled device detector (Spex CCD) cooled by Peltier effect to 200 K. A He:Ne laser (632.8 nm) was used as the excitation source. The spectra were measured in back-scattering geometry. The resolution was about 0.5 cm^{-1} . A 100 \times objective was used to focus the laser light on sample surface to a spot size of $1 \mu\text{m}^2$. The power of the laser beam was adjusted to 0.2–0.5 mW with neutral filters of various optical densities in order to prevent local heating of the sample. Raman spectra were systematically recorded on 10 different spots of each sample to check the homogeneity. The morphology of the LMNO powder was characterized by scanning electron microscopy (SEM), Zeiss, Merlin-type microscope. Energy Dispersive X-ray Spectroscopy (EDS) analysis was applied to determine the elemental composition together with SEM with an accelerating voltage of 10–15 kV.

Electrochemical tests

The positive electrode is prepared by mixing 80 wt% of active material (LMNO powder) with 15 wt% of carbon black (Alfa Aesar, 99+ %) and 5 wt% of PTFE (Fluka chemicals) as binder. About 6 mg of this mix is pressed on a 16 mm stainless steel current collector. Li metal (Alfa Aesar, 99.9%, metal basis) was used as negative electrode. CR2032 coin cells were assembled in an argon-filled inert atmosphere glovebox (<0.5 ppm of H₂O and <0.5 ppm of O₂). The two electrodes are separated by a Whatmann glass fiber soaked in the electrolyte. The electrolyte solution was battery grade 1 M LiPF₆ dissolved in ethylene carbonate: dimethyl carbonate (EC: DMC), 1:1 vol. % (Sigma Aldrich). Electrochemical experiments were performed at 20°C using a VMP3 Biologic apparatus.

The structural investigation was carried out in the 3.5 V – 4.9 V potential window by using two electrodes coin cells, during the second charge-discharge cycle of LMNO. The cells were charged (and discharged) at C/10 rate up to the required x composition in L_{1-x}MNO ($0 \leq x < 1$), by maintaining the cell at the required voltage until the current through the cell was not changing more than $2 \mu\text{A/h}$. The cells were then disassembled in the glove box. The positive electrodes were rinsed 3 times with DMC in order to remove any electrolyte residues and placed in appropriate airtight sample holders to be further analysed by XRD and Raman spectroscopy.

For self-discharge study, after being completely charged at 4.9 V, the cells were kept at zero current for varying rest times (10,

20 and 30 days). Then, they were disassembled and the positive electrodes were cleaned by DMC three times and analysed by Raman. At the same time, a second batch of cells were fully charged and kept in same ageing time conditions (10, 20 and 30 days rest), then discharged to estimate the capacity loss.

Authors Contribution

Ankush Bhatia: Investigation, Validation, Visualisation, Writing-Original draft

Yosra Dridi: Investigation

Jean-Pierre Pereira-Ramos: Project administration, Conceptualization, Writing-review & editing, funding acquisition

Rita Baddour-Hadjean: Project administration, Conceptualization, Methodology, Supervision, Formal analysis Writing-review & editing, funding acquisition

Conflicts of interest

There are no conflicts to declare.

Acknowledgements

The authors acknowledge the French ANR project "CASSIOPES" N°17-CE09-0016-03 for their financial support, Dr. N. Emery for his help on XRD and neutron analysis and Dr R. I. Smith, ISIS Facility, STFC Rutherford Appleton Laboratory, UK, for neutron diffraction experiments. Experiments on GEM at the ISIS Pulsed Neutron and Muon Source were supported by a beam time allocation from the Science and Technology Facilities Council using the GEM XPRESS Service (XB1890380).

References

- J. M. Tarascon and M. Armand, *Nature*, 2001, **414**, 359.
- B. Diouf and R. Podes, *Renew. Energy*, 2015, **76**, 375
- J. B. Goodenough and Y. Kim, *Chem. Mater.*, 2010, **22**, 587.
- M. M. Thackeray, W. I. F. David, P. G. Bruce and J. B. Goodenough, *Mater. Res. Bull.*, 1983, **18**, 461.
- O. K. Park; Y. Cho; S. Lee, H. C. Yoo, H. K. Song and J. Cho, *Energy Environ. Sci.*, 2011, **4**, 1621.
- J. H. Kim, N. P. Pieczonka and L. Yang, *Chem. Phys. Chem.*, 2014, **15**, 1940.
- A. Yamada, M. Tanaka, K. Tanaka and K. Sekai, *J. Power Sources*, 1999, **81-82**, 73.
- T. Ohzuku, S. Takeda and M. Iwanaga, *J. Power Sources*, 1999, **81-82**, 90.
- K. Amine, H. Tukamoto, H. Yasuda and Y. Fujita, *J. Electrochem. Soc.*, 1996, **143**, 1607.
- S. Patoux, L. Sannier, H. Lignier, Y. Reynier, C. Bourbon, S. Jouanneau, F. Le Cras and S. Martinet, *Electrochim. Acta*, 2008, **53**, 4137.
- W. Du, N. Xue, A.M. Sastry, J.R.R.A. Martins and W. Shyy, *J. Electrochem. Soc.*, 2013, **160**, A1187.
- J. H. Kim, C. S. Yoon, S. T. Myung, J. Prakash and Y. K. Sun, *Electrochem. Solid State Lett.*, 2004, **7**, A216.
- J. Lu and K. S. Lee, *Mater. Technol.*, 2016, **31**, 628.
- A. Manthiram, K. Chemelewski and E. S. Lee, *Energy Environ. Sci.*, 2014, **7**, 1339.
- L. Yang, B. Ravdel and B. L. Lucht, *Electrochem. Solid State Lett.*, 2010, **13**, A95.
- W. M. Seong, K. Y. Park, M. H. Lee, S. Moon, K. Oh, H. Park, S. Lee and K. Kang, *Energy Environ. Sci.*, 2018, **11**, 970.
- S. Patoux, L. Daniel, C. Bourbon, H. Lignier, C. Pagano, F. Le Cras, S. Jouanneau and S. Martinet, *J. Power Sources*, 2009, **189**, 344.
- X. L. Xu, S. X. Deng, H. Wang, J. B. Liu and H. Yan, *Nano-Micro Lett.* 2017, **9**, 22.
- A. Kraysberg, H. Drezner, M. Auinat, A. Shapira, N. Solomatin, P. Axmann, M. Wohlfahrt-Mehrens and Y. Ein-Eli, *ChemNanoMat*, 2015, **1**, 577.
- G. Gabrielli, P. Axmann, T. Diemant, J. Behm and M. Wohlfahrt-Mehrens, *ChemSusChem*, 2016, **9**, 1670.
- M. Xu, L. Zhou, Y. Dong, Y. Chen, J. Demeaux, A.D. MacIntosh, A. Garsuch, B. L. Lucht, *Energy Environ. Sci.*, 2016, **9**, 1308.
- A. von Cresce and K. Xu, *J. Electrochem. Soc.* 2011, **158**, A337.
- M. Marcinek, J. Syzdek, M. Marczewski, M. Piszcz, L. Niedzicki, M. Kalita, A. Plewa-Marczewska, A. Bitner, P. Wiczorek, T. Trzeciak, M. Kasprzyk, P. Lezak, Z. Zukowska, A. Zalewska and W. Wiczorek, *Solid State Ionics*, 2015, **276**, 107.
- J. C. Fang, Y. F. Xu, G. L. Xu, S. Y. Shen, J. T. Li, L. Huang and S. G. Sun, *J. Power Sources*, 2016, **304**, 15.
- G. Gabrielli, P. Axmann and M. Wohlfahrt-Mehrens, *J. Electrochem. Soc.* 2016, **163**, A470.
- P. Axmann, G. Gabrielli and M. Wohlfahrt-Mehrens, *J. Power Sources*, 2016, **301**, 151.
- J. Liu and A. Manthiram, *Chem. Mater.*, 2009, **21**, 1695.
- S. T. Myung, S. Komaba, N. Kumagai, H. Yashiro, H. T. Chung and T. H. Cho, *Electrochim. Acta*, 2002, **47**, 2543.
- R. Alcántara, M. Jaraba, P. Lavela and J. L. Tirado, *Electrochim. Acta*, 2002, **47**, 1829.
- J. H. Kim, S. T. Myung, C. S. Yoon, S. G. Kang and Y. K. Sun, *Chem. Mater.*, 2004, **16**, 906.
- M. Kunduraci and G. G. Amatucci, *J. Electrochem. Soc.*, 2006, **153**, A1345.
- L. Wang, H. Li, X. Huang and E. Baudrin, *Solid State Ionics*, 2011, **193**, 32.
- J. Zheng, J. Xiao, X. Yu, L. Kovarik, M. Gu, F. Omenya, X. Chen, X.Q. Yang, J. Liu, G. L. Graff, M. S. Whittingham and J. G. Zhang, *Phys. Chem. Chem. Phys.*, 2012, **14**, 13515.
- H. Duncan, B. Hai, M. Leskes, C. P. Grey and G. Chen, *Chem. Mater.*, 2014, **26**, 5374.
- W. K. Pang, N. Sharma, V. K. Peterson, J. J. Shiu and S. H. Wu, *J. Power Sources*, 2014, **246**, 464.
- H. Komatsu, H. Arai, Y. Koyama, K. Satp, T. Kato, R. Yoshida, H. Murayama, I. Takahashi, Y. Orikasa, K. Fukuda, T. Hirayama, Y. Ikuhara, Y. Ukyo, Y. Uchimoto and Z. Ogumi, *Adv. Energy Mater.*, 2015, **5**, 1500638.
- J. Lee, C. Kim and B. Kang, *NPG Asia Mater.*, 2015, **7**, e211.
- P. B. Samarasingha, J. Sottmann, S. Margadonna, H. Emerich, O. Nilsen and H. Fjellvåg, *Acta Mater.*, 2016, **116**, 290.
- Y. J. Lee, C. Eng and P. C. Grey, *J. Electrochem. Soc.*, 2001, **148**, A249.
- K. Shimoda, M. Murakami, H. Komatsu, H. Arai, Y. Uchimoto, and Z. Ogumi, *J. Phys. Chem. C*, 2015, **119**, 13472.
- R. Alcántara, M. Jaraba, P. Lavela, J. L. Tirado, E. Zhecheva and R. Stoyanova, *Chem. Mater.*, 2004, **16**, 1573.
- R. Baddour-Hadjean and J.P. Pereira-Ramos, *Chem. Rev.*, 2010, **110**, 1278.

- 43 E. Flores, P. Novák and E. J. Berg, *Front. Energy Res.* 2018, **6**, 82.
- 44 C.M. Julien and A. Mauger, *AIMS Mater. Sci.* 2018, **5**, 650.
- 45 R. Baddour-Hadjean, S. Bach, M. Smirnov and J. P. Pereira-Ramos, *J. Raman Spectrosc.* 2004, **35**, 577.
- 46 R. Baddour-Hadjean, C. Navone, J. P. Pereira-Ramos, *Electrochim. Acta*, 2009, **54**, 6674.
- 47 R. Baddour-Hadjean, A. Marzouk and J. P. Pereira-Ramos, *J. Raman Spectrosc.* 2012, **43**, 153.
- 48 M. B. Smirnov, E. M. Roginskii, V. Yu. Kazimirov, K. S. Smirnov, R. Baddour-Hadjean, J. P. Pereira-Ramos and V. S. Zhandun, *J. Phys. Chem. C*, 2015, **119**, 20801.
- 49 J. Lei, F. McLarnon and R. Kostecki, *J. Phys. Chem. B* 2005, **109**, 952.
- 50 J. Nanda, J. Remillard, A. O'Neill, D. Bernardi, T. Ro, K. E. Nietering, J.-Y. Go and T. Miller, *Adv. Funct. Mater.* 2011, **21**, 3282.
- 51 E. Flores, N. Vonrüti, P. Novak, U. Aschauer and E. J. Berg, *Chem. Mater.* 2018, **30**, 4694.
- 52 C. V. Rao, J. Soler, R. Katiyar, J. Shojan, W. C. West and R. S. Katiyar, *J. Phys. Chem. C* 2014, **118**, 14133.
- 53 R. E. Ruther, A. F. Callender, H. Zhou, S. K. Martha and J. Nanda, *J. Electrochem. Soc.* 2015, **162**, A98.
- 54 E. Flores, P. Novak, U. Aschauer and E. J. Berg, *Chem. Mater.* 2020, **32**, 186.
- 55 P. Lanz, C. Villevieille and P. Novak, *Electrochim. Acta* 2014, **130**, 206.
- 56 W. Zhu, D. Liu, J. Trottier, C. Gagnon, J. Howe, A. Mauger, C. M. Julien and K. Zaghbi, *J. Power Sources*, 2015, **298**, 341.
- 57 K. Dokko, M. Mohamedi, N. Anzue, T. Itoh and I. Uchida, *J. Mater. Chem.*, 2002, **12**, 3688.
- 58 D. Liu, J. Han and J. B. Goodenough, *J. Power Sources*, 2010, **195**, 2918.
- 59 J. Cabana, M. Casas-Cabanas, F. O. Omenya, N. A. Chernova, D. Zeng, M. S. Whittingham and C. P. Grey, *Chem. Mater.*, 2012, **24**, 2952.
- 60 Y. Dridi Zrelli, Thèse Université Paris-Est, 2012. Français. NNT: 2012PEST1126
- 61 A. Bhatia, J. P. Pereira-Ramos, N. Emery, B. Laïk, R. I. Smith, and R. Baddour-Hadjean, *ChemElectroChem*, 2020, **7**, 3420.
- 62 C. Julien, F. Gendron, A. Amdouni and M. Massot, *Mater. Sci. Eng. B*, 2006, **130**, 41.
- 63 C. M. Julien and M. Massot, *Mater. Sci. Eng. B*, 2003, **97**, 217.
- 64 Ammundsen, G. R. Burns, M. S. Islam, H. Kanoh and J. Roziere, *J. Phys. Chem B*, 1999, **103**, 5175.
- 65 L. Boulet-Roblin, C. Villevieille, P. Borel, C. Tessier, P. Novák, and M. Ben Yahia, *J. Phys. Chem. C*, 2016, **120**, 16377.
- 66 W. B. White and B. A. DeAngelis, *Spectrochim. Acta A*, 1967, **23**, 985.
- 67 G. T. K. Fey, C. Z. Lu and T. P. Kumar, *J. Power Sources*, 2003, **115**, 332.
- 68 J.-H. Kim, A. Huq, M. Chi, N. P. W. Pieczonka, E. Lee, C. A. Bridges, M. M. Tessema, A. Manthiram, K. A. Persson and B. R. Powell, *Chem. Mater.*, 2014, **26**, 4377.
- 69 D. Liu, W. Zhu, J. Trottier, C. Gagnon, F. Barry, A. Guerfi, A. Mauger, H. Groult, C. M. Julien, J. B. Goodenough and K. Zaghbi, *RSC Adv.*, 2014, **4**, 154.
- 70 M. Kunduraci and G. G. Amatucci, *J. Power Sources*, 2007, **165**, 359.
- 71 J. Song, D. W. Shin, Y. Lu, C. D. Amos, A. Manthiram and J. B. Goodenough, *Chem. Mater.*, 2012, **24**, 3101.
- 72 W. H. Kan, S. Kuppan, L. Cheng, M. Doeff, J. Nanda, A. Huq, and G. Chen, *Chem. Mater.*, 2017, **29**, 6818.
- 73 M. Bianchini, F. Fauth, E. Suard, J. N. Leriche, C. Masquelier and L. Croguennec, *Acta Cryst B*, 2015, **71**, 688.
- 74 A. C. Larson, R. B. Von and D. Lansce, General Structure Analysis System (GSAS), Los Alamos National Laboratory, Technical Report No. LAUR86-748, 2004.
- 75 B. H. Toby, *J. Appl. Crystallogr.*, 2001, **34**, 210.
- 76 S. Hull, R. I. Smith, W. I. F. David, A. C. Hannon, J. Mayers and R. Cywinski, *Phys. B Phys. Condens. Matter.*, 1992, **180-181**, 1000.